JOURNAL OF MATERIALS SCIENCE 33(1998) 319–327

Load-adaptive crystalline–amorphous nanocomposites

A. A. VOEVODIN, J. S. ZABINSKI
Materials Directorate, Wright Laboratory, Wright–Patterson Air Force Base, OH 45433-7750, USA

Advances in laser-assisted deposition have enabled the production of hard composites consisting of nanocrystalline and amorphous materials. Deposition conditions were selected to produce super-tough coatings, where controlled formation of dislocations, nanocracks and microcracks was permitted as stresses exceeded the elastic limit. This produced a self-adjustment in the composite deformation from hard elastic to quasiplastic, depending on the applied stress, which provided coating compliance and eliminated catastrophic failure typical of hard and brittle materials. The load-adaptive concept was used to design super-tough coatings consisting of nanocrystalline (10–50 nm) TiC grains embedded in an amorphous carbon matrix (about 30 vol%). They were deposited at near room temperature on steel surfaces and studied using X-ray photoelectron spectroscopy, X-ray diffraction, scanning electron microscopy, Raman spectroscopy, nanoindentation and scratch tests. Design concepts were verified using composition–structure–property investigations in the TiC–amorphous carbon (a-C) system. A fourfold increase in the toughness of hard (32 GPa) TiC–a-C composites was achieved in comparison with nanocrystalline single-phase TiC.

1. Introduction

Recent reports showed the possibility of producing nano-phase composites, where the crystalline phase was embedded in an amorphous matrix. This created a barrier to dislocations and dramatically increased the hardness of the material [1, 2]. In these reports, a chemical vapour deposition technique was used, which required high substrate temperatures, i.e., 500–600 °C, to promote growth of a crystalline phase. For a variety of applications, e.g., bearing balls, races and gears, a low process temperature is required to prevent substrate distortion and loss of mechanical properties. Another requirement for engineering coatings is resistance to brittle fracture at deformations exceeding the elastic limit, i.e., a high toughness. For wear protection, a low friction coefficient is also very important.

Crystalline carbide–amorphous carbon (a-C) composites have the potential to provide both a hard and low-friction coating. They could be realized using metal carbides with excess carbon. The Ti–C material system is one of the most promising. The possibility for segregation of an a-C phase in super-stoichiometric TiC was reported more than a decade ago by Sundgren *et al.* [3] for reactive sputtering with a relatively high substrate temperature (500 °C). Recently, Knotek *et al.* [4] investigated super-stoichiometric carbides produced at 180 °C, which had friction coefficients as low as 0.2. However, a decrease from the maximum hardness of 20–25 GPa for stoichiometric TiC was found with increasing carbon content [4].

In other sputtering developments, titanium was doped into a diamond-like carbon (DLC) matrix to segregate TiC grains [5–7]. These composites had better mechanical properties than DLC and had friction coefficients of about 0.1. However, their hardness did not exceed 15 GPa owing to hydrogenation of the DLC matrix.

More recently, magnetron sputtering-assisted pulsed-laser deposition (MSPLD) was used to grow crystalline carbides and carbonitrides from independent sources of carbon and metal plasmas at substrate temperatures as low as 100 °C [8, 9]. Laser ablation of graphite produces hydrogen-free DLC with a hardness of about 60–70 GPa and a friction coefficient below 0.1 [10–12]. Addition of a Ti plasma in MSPLD and control over the ratio of C and Ti fluxes made possible the preparation of TiC and hard a-C with different degrees of Ti doping [8, 13]. Fig. 1 shows the non-equilibrium phase transitions in the Ti–C coatings deposited by MSPLD [13]. In contrast with equilibrium phase formation, crystalline TiC and a-C phases were observed over a wide range of compositions.

The objective of this research was to develop tough TiC–a-C composites by adjusting the size of carbide nanocrystallites and the volume fraction of a-C matrix. Design concepts for supertoughness (and not superhardness) were suggested and verified on coatings produced by MSPLD after detailed studies of the TiC → DLC transition.

0022–2461

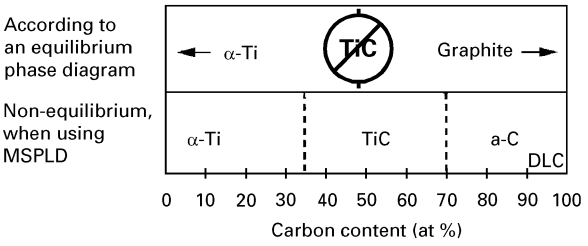

Figure 1 Comparison of phases existing in the Ti-C system prepared at near room temperatures in equilibrium and non-equilibrium MSPLD conditions.

2. Conceptual design of tough crystalline–amorphous composites

Hard materials have high elastic moduli and do not plastically deform to a significant degree; therefore, they are usually brittle. A super-hard coating may not be an ideal choice for many cases of wear protection, where stresses above the elastic limit are experienced e.g., micron-sized asperities and hard particles in sliding or rolling contacts. The danger of catastrophic fracture can be considerably reduced if the coating is hard and elastic at normal operating loads, and plastically compliant at higher or extreme loads. The change of behaviour from elastic to plastic can provide stress relaxation and distribute the localized load over larger volumes.

In composites, plasticity can be introduced either by plastic deformation in one of the phases or by grain boundary deformation similar to superplasticity in nanocrystalline ceramics and oxides [14–16]. For composites consisting of hard phases, a controlled development of nanocracks and microcracks along phase boundaries can be used to obtain grain shifts and to achieve unrecoverable pseudoplasticity. This approach removes some constraints of superhard composite designs, which require 3–4 nm grain sizes with less than 1 nm separation [2].

First, crystalline grains can be increased to a size, which is sufficient for dislocation formation but smaller than the critical size of a self-propagating crack at the applied stress. For a variety of wear protective coatings, contact stresses are in the range 10^8–10^{10} Pa, e.g., journal and rolling bearings. If a localized stress of 1 GPa is used as an average, then a self-propagating crack from Griffith's criteria is in the range of 50–100 nm for materials with elastic moduli of 200–400 GPa and the adhesion work for crack opening is about 1 J m^{-2} [17].

Second, the separation of crystallites in an amorphous matrix can be increased to relax incoherence stress and to permit non-catastrophic nanocracks along grain boundaries. For most materials, incoherence stresses relax to negligible values for interface thicknesses above four to five crystal lattice periods or 1–3 nm [2].

From these considerations, the following design criteria were selected.

(i) The size of a crystalline phase needs to be between 5 and 50 nm to permit dislocation formation but to prevent development of self-propagating cracks.

(ii) Crystallite separation in an amorphous matrix needs to be about 5 nm. This requires about 30 vol% of amorphous phase, when using TiC crystalline spheres of 50 nm diameter packed with 5 nm separation and voids filled with a-C.

3. Experimental procedure

Composite coatings of 0.5 μm thickness were grown on type 440C stainless steel discs of 24.5 mm diameter. Substrates were polished to $R_a = 0.02$ μm, ultrasonically cleaned in acetone and placed in a vacuum below 10^{-6} Pa. The deposition temperature was 50–70 °C, resulting from substrate etching in an Ar plasma to remove surface oxides. MSPLD without substrate heating or biasing was used. A carbon flux produced by excimer laser ablation of graphite was intersected with a titanium flux produced by magnetron sputtering at an Ar background pressure of 0.3 Pa. Film stoichiometry was regulated with the laser pulse frequency, keeping all other deposition parameters constant. Details of the MSPLD configuration, deposition parameters and control have been provided in [8, 13].

The coating surface morphology was investigated with a Cambridge Stereoscan field emission scanning electron microscope without applying metal overcoats. Images were analysed to find an average grain size.

Coating composition and chemical bonding were investigated using X-ray photoelectron spectroscopy (XPS) (Surface Science Instruments M-Probe instrument). Monochromatic Al Kα X-rays were used to give a full width at half-maximum of 0.77 eV for the Au 4f 7/2 peak at 25 eV pass energy and 400 μm × 1000 μm spot. Relative peak areas were used for compositional quantification and were corrected for a spectrometer factor and X-ray cross-section. Sintered stoichiometric TiC and graphite discs were used for final calibration. Electron escape depth variations for different elements were neglected. A 4 keV Ar gun was used for 15 s to remove hydrocarbon and hydroxyl surface contaminants absorbed during sample transfer in laboratory air.

The microstructure of TiC was analysed by grazing-angle X-ray diffraction (XRD) using a Rigaku D-MAXB thin-film XRD system with a Cu Kα X-ray source operating at a 5° incidence angle. Broadening of diffraction peaks was used to evaluate the crystalline size. Instrumental broadening was corrected using XRD patterns obtained from a TiC standard at the same conditions. The microstructure of a-C was analysed with Raman spectroscopy using a 514.5 nm laser.

Hardnesses and Young's moduli were measured with a Nanoindenter IIs microprobe. A Berkovich indenter was loaded in the range of 1 mN. Hardness was found for the maximum penetrations, and moduli were calculated from the upper unloading portions of the load–displacement curves as described in [18].

Toughness was evaluated with a CSEM scratch tester, using a diamond tip of 0.2 mm radius dragged at a constant speed of 5 mm min^{-1} on the coating

surface. The normal load was linearly increased from 0 to 100 N at a rate of 50 N min^{-1}. Bursts of acoustic emission were used to determine crack developments and gave a lower critical load; changes in the tangential frictional force were used to determine tip penetration to the substrate and provided an upper critical load [19]. Optical and scanning electron microscopy (SEM) images were used to interpret the results of scratch tests.

4. Results and discussion

4.1. Characterization of TiC–a-C composites

Composites prepared for this study are listed in Table I together with results of XPS analyses of their stoichiometric and phase compositions. The low oxygen content (3–9 at%) originated from surface oxidation in the laboratory atmosphere. The oxygen content could be reduced by longer Ar bombardment, which was not performed to escape surface alteration. The ratio of titanium to carbon was used to designate the samples.

With an increase of carbon content, a transition from TiC to a-C was observed via formation of super-stoichiometric TiC, two-phase TiC–a-C, titanium-doped a-C (Ti: a-C), and a-C (Fig. 2). The TiC → a-C transition was quantified by estimating the ratio of carbon bonded in TiC and a-C. For this, the positions of the C 1s peaks at 281.8 eV (TiC) and 284.6 eV (a-C) were locked, the peaks were fitted with Voight functions, and their area ratios were calculated. The results are presented in Table I, which shows how the segregation of a-C phase suppresses TiC formation at high carbon contents after a two-phase a-C–TiC region at 60–80 at% C.

From XRD analyses, a crystalline TiC phase was formed at carbon contents of up to 80 at% before coatings became X-ray amorphous. Five TiC diffraction peaks corresponding to (1 1 1), (2 0 0), (2 2 0), (3 1 1) and (2 2 2) hexagonal close packed were

TABLE I Results of XPS investigations of TiC–a-C composites: Ti–C stoichiometries, chemical compositions and percentages of carbon bonded in a-C and TiC phases

Ti–C	Chemical composition (at %)			Amount of C (%) bonded into the following	
stoichiometry	Ti	C	O	a-C	TiC
$Ti_{0.45}C_{0.55}$	41	50	9	15	85
$Ti_{0.41}C_{0.59}$	37	54	9	22	78
$Ti_{0.37}C_{0.63}$	34	58	8	29	71
$Ti_{0.36}C_{0.64}$	33	58	9	35	65
$Ti_{0.34}C_{0.66}$	31	61	8	45	55
$Ti_{0.32}C_{0.68}$	29	62	9	50	50
$Ti_{0.28}C_{0.72}$	26	67	7	67	33
$Ti_{0.25}C_{0.75}$	23	69	8	73	27
$Ti_{0.19}C_{0.81}$	18	76	6	87	13
$Ti_{0.18}C_{0.82}$	17	78	5	90	10
$Ti_{0.16}C_{0.84}$	15	79	6	96	4
$Ti_{0.14}C_{0.86}$	13	83	4	98	2
$Ti_{0.09}C_{0.91}$	9	88	3	99	1
DLC	0	100	< 0.5	100	< 0.5

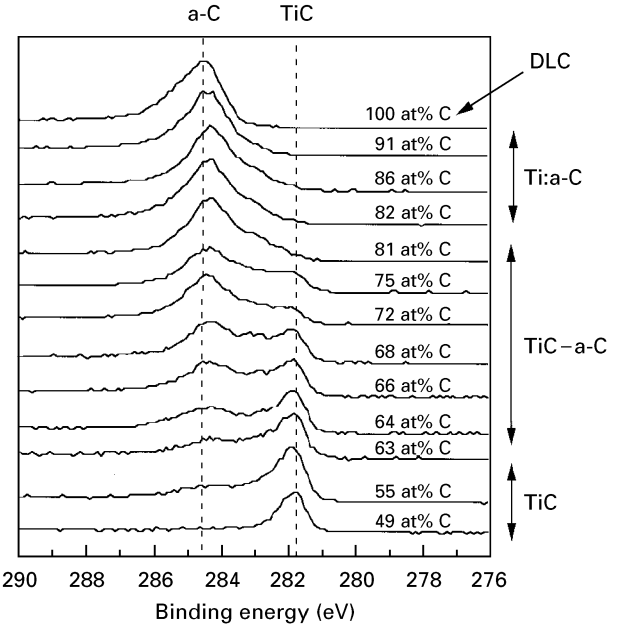

Figure 2 XPS results for C 1s binding energy variations for the TiC → a-C phase transition occurring as the carbon content is increased.

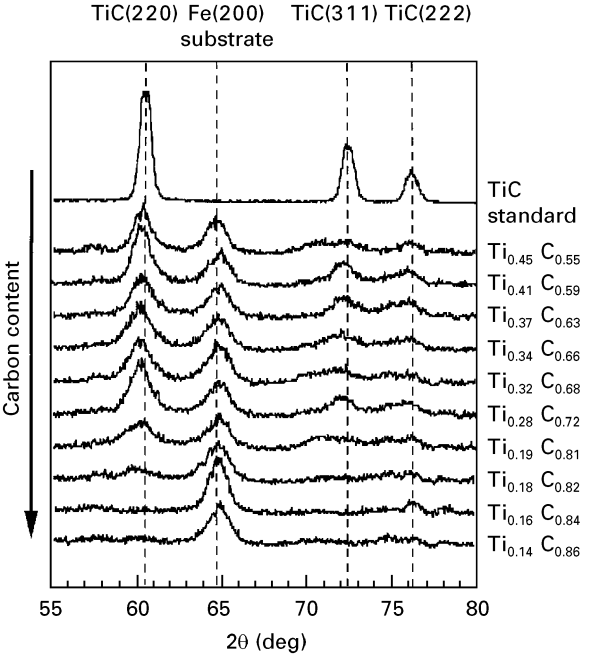

Figure 3 Comparison of diffraction spectra for Ti–C coatings with different carbon contents and the TiC standard.

observed without dominant texturing. Large angle diffraction peaks are shown in Fig. 3 in comparison with a diffractogram from the TiC standard. An increased peak width for Ti–C coatings is immediately clear (Fig. 3). This broadening was due to size effects and/or high levels of point defects. The peak positions were not shifted with respect to the standard (Fig. 3), indicating negligible macrostresses.

Coatings with carbon content above 75 at% had sufficient amounts of the a-C phase to produce Raman scattering (Fig. 4). Interpretation of spectra was accomplished using graphite scatter bands at 1580 cm^{-1}

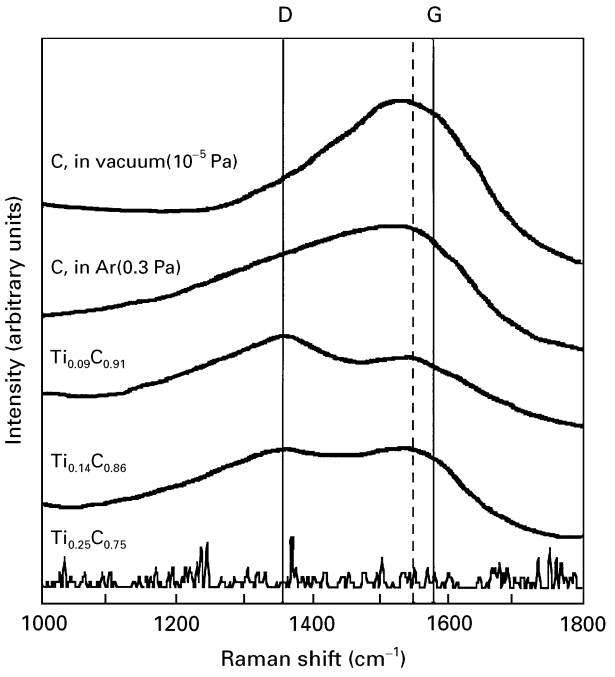

Figure 4 Comparison of Raman spectra for titanium doped a-C coatings and pure carbon coatings. The solid vertical lines indicate the positions of the D and G peaks for polycrystalline graphite, and the broken vertical line indicates the position of a single G maximum typically observed for DLC.

(G band) and at 1357 cm^{-1} (D band), and the single scatter G band at 1550 cm^{-1}, which is typically assigned to DLC [20–22].

The shift in the G peaks to lower frequencies than 1580 cm^{-1} indicated that the a-C phase was not graphite (Fig. 4). However, for Ti: a-C coatings, both G and D bands were nearly equal in intensity and produced a broad maximum. Interpretations of similar Raman spectra suggested that graphite-like sp^2 bonds were present, together with diamond-like sp^3 bonds [23, 24]. Coatings deposited without Ti had a single maxima at 1540 cm^{-1} representing sp^3-bonded DLC [25].

An interesting feature of TiC–a-C coatings was the change in surface morphology with increased carbon content (Fig. 5). Coatings with predominantly TiC phase, i.e., carbon content below 70 at% from Table I, exhibited well-defined and sharp nanograins. Coatings with predominantly a-C phase, i.e. above 70 at% C, exhibited spherical grains, which became less densely packed at carbon contents above 90 at%. From the combined results of XPS, XRD and Raman studies, this morphology change can be explained by a-C phase segregation on borders between TiC nanocrystals. As the carbon content increases, the formation of a-C suppresses the growth of TiC crystals, encapsulates TiC grains and, eventually, reduces the number of TiC grains, providing their rounded appearance and less dense packing.

Sizes of TiC crystals were within a defined range, with the lower limit estimated from XRD broadening, neglecting contribution from point defects, and the upper limit estimated from grain sizes observed in

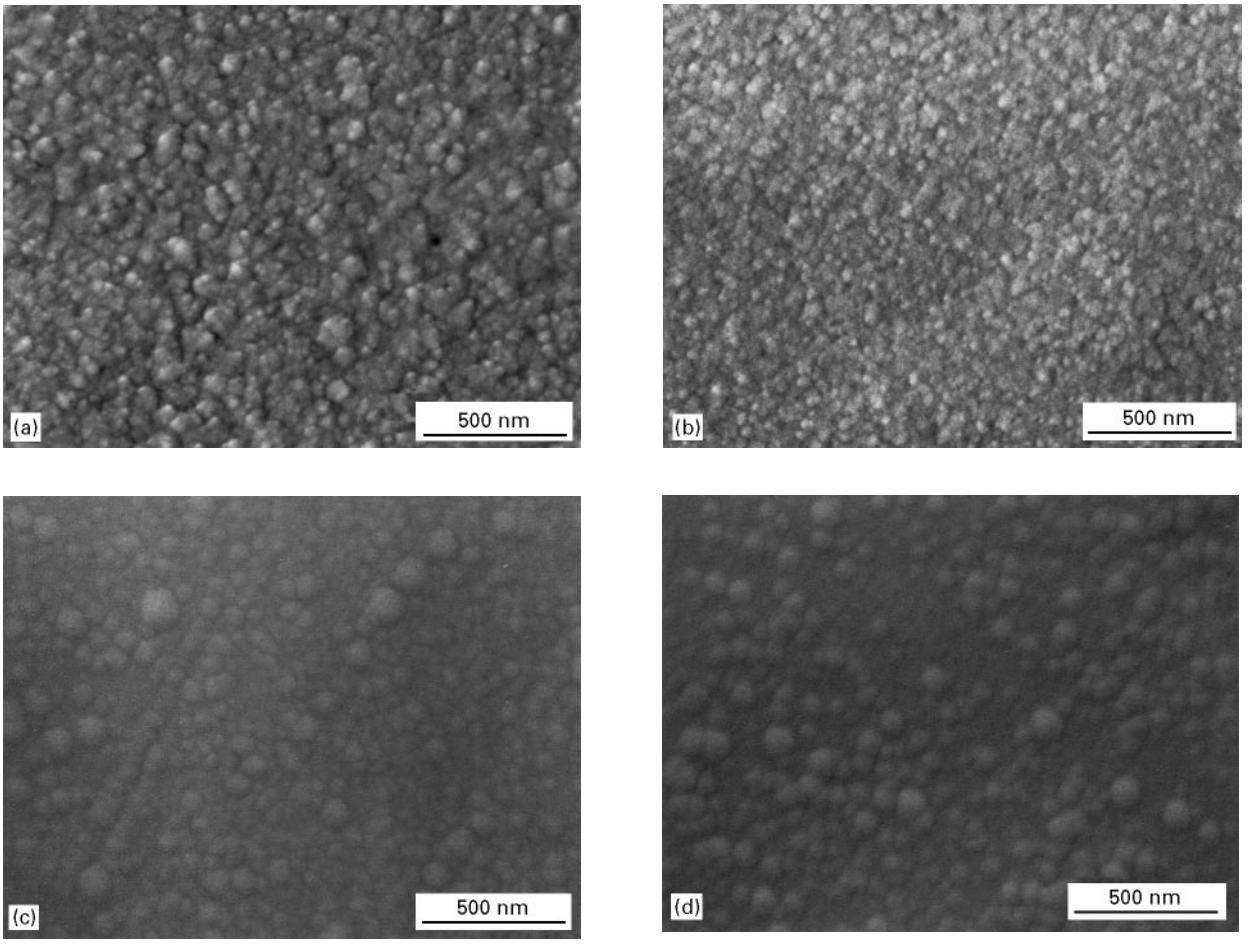

Figure 5 High-resolution SEM images of surface morphology of TiC–a-C composite coatings with different carbon contents: (a) 63 at%; (b) 68 at%; (c) 75 at%; (d) 92 at%.

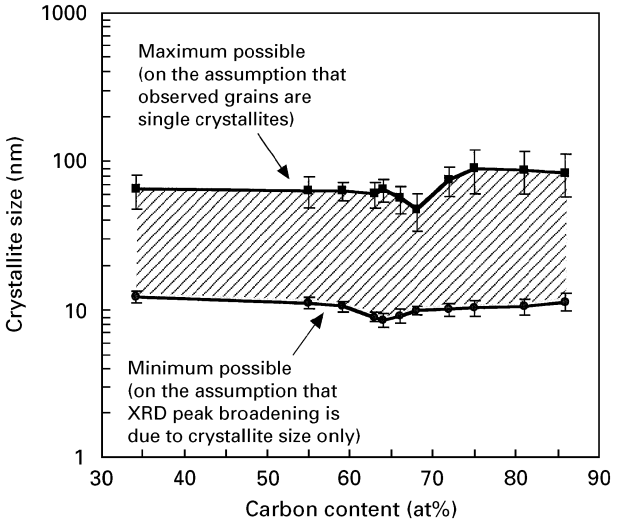

Figure 6 Range of possible sizes of TiC crystallites in TiC–a-C composite coatings determined from XRD (●) and SEM (■) data for different carbon contents.

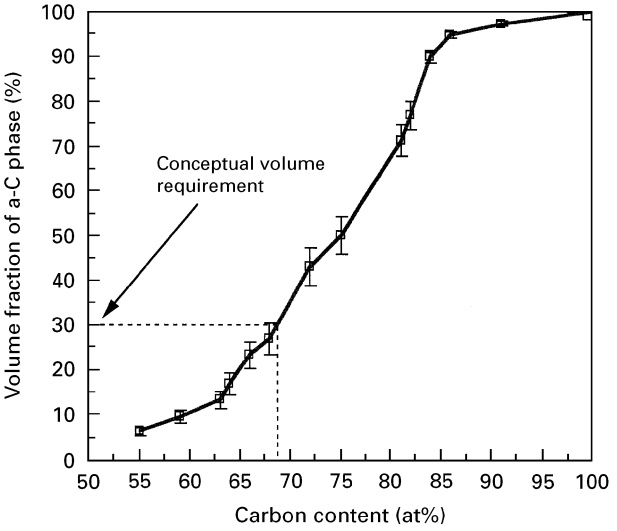

Figure 7 Variation in volume fraction of a-C phases in TiC–a-C composites as a function of carbon content. The error bars reflect the uncertainty in the a-C density which could be from 2.2 g cm^{-3} (graphite) to 3.1 g cm^{-3} (DLC).

SEM, approximating grains as single TiC crystallites. These estimates provided a size range of 10–80 nm as shown in Fig. 6. There was also a minimum in size at 65–70 at% C, which was attributed to suppressing TiC crystal formation with the a-C precipitation. For coatings with carbon content above 70 at%, the upper limit in Fig. 6 is overestimated, since segregation of a-C increased apparent grain sizes in SEM imaging.

4.2. Composites with structure corresponding to a supertoughness concept

Structural characterizations are summarized in Table II, which helped to match the produced composites with the design criteria of Section 2.

(i) The size range of TiC nanocrystals in all investigated composites was close to the required 10–50 nm.

(ii) The 30 vol% a-C phase was achieved at an atomic carbon content of about 70 at% (Fig. 7). The a-C volume fractions were calculated from the percentage of carbon bonded in TiC and a-C (Table I). A density of 4.93 g cm^{-3} was used for TiC [26], and the density of a-C was varied from 2.25 g cm^{-3} for graphite [26] to 3.1 g cm^{-3} for DLC produced by pulsed-laser deposition [12].

Composites with about 70 at% C were also found to have the required 5 nm separation between TiC grains, when carbide crystals were approximated by spherical particles with averaged sizes derived from XRD and SEM analyses (Fig. 8). Therefore, they had the best match to the tough composite design, with the $Ti_{0.32}C_{0.68}$ coating having the closest composition to the design optimum.

TABLE II Summary results of structural characterizations of TiC–a-C composites with various carbon content

Carbon content (at%)	Structure (schematic)	Composite description	TiC crystal size (nm)	a-C phase volume (%)	a-C interface thickness (nm)
55–65		Consists of TiC grains with a minor amount of secondary a-C phase	10–70	5–20	1–2
65–70		Significant amount of a-C phase formed between TiC crystallites	10–50	20–30	2–5
70–80	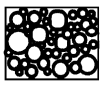	Densely packed TiC grains encapsulated in a-C, providing grains of spherical shape	20–90	30–60	5–12
80–100	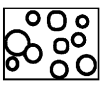	Random inclusion of TiC grains encapsulated into an a-C matrix	20–100	60–100	> 12

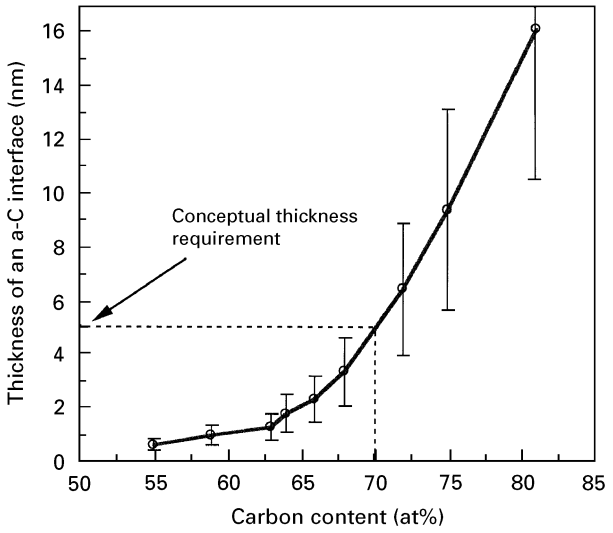

Figure 8 Variation in thickness of the a-C interface between TiC nano crystals in TiC–a-C composites as a function of carbon content. The error bars are due to the discrepancy in the calculations owing to the difference in TiC crystal size estimations from XRD and SEM data.

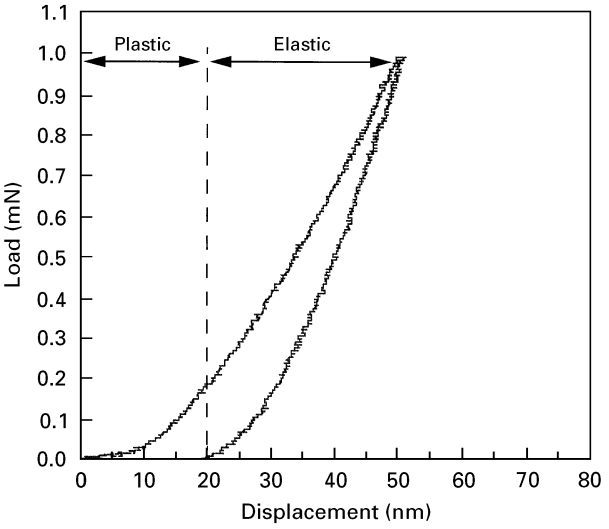

Figure 10 A typical loading–unloading nanoindentation curve for the $Ti_{0.32}C_{0.68}$ coating. The calculated mechanical properties, are as follows: maximum hardness, 32 GPa; elastic modulus, 370 GPa; elastic recovery, 60%.

4.3. Hardness and toughness of TiC–a-C composites

Fig. 9 presents the variation in TiC–a-C hardness as a function of carbon content. The maximum hardness of 32 GPa was found in the range 65–75 at% C. The increase was about 50% above the hardness of stoichiometric TiC coatings and was lower than that reported for superhard composites [1, 2].

In nanoindentation experiments, approximately 40% plastic deformation occurred for the $Ti_{0.32}C_{0.68}$ coating (Fig. 10). Such plastic compliance is quite high for a hard coating, in comparison with 10% plastic deformation for 60–70 GPa hard DLC [11, 12], or the absence of plasticity in superhard composites [2]. The elastic modulus of the $Ti_{0.32}C_{0.68}$ coating was about 370 GPa, which is below the 600 and 500 GPa values reported for DLC and superhard composites, respectively [2, 11]. Thus, TiC–a-C coatings had much more plasticity than superhard materials did, demonstrating the validity of the design concept.

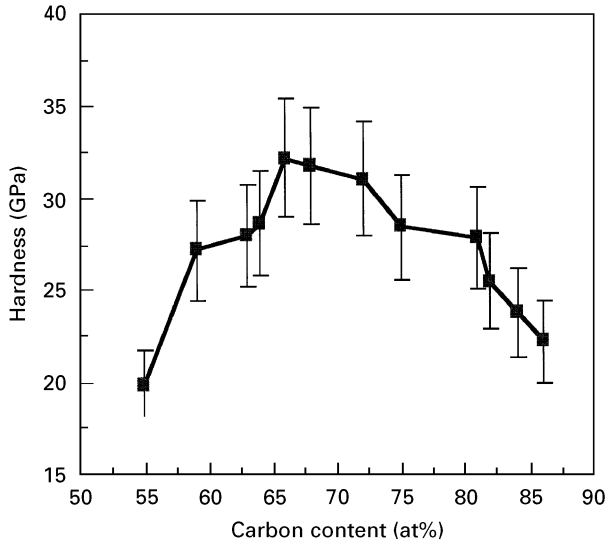

Figure 9 Hardness variation for TiC–a-C composites as a function of carbon content.

In scratch experiments, a critical dependence of coating performance on the composition was clearly present with a remarkable plastic compliance of the $Ti_{0.32}C_{0.68}$ coating (Fig. 11). A very high toughness of the TiC–a-C coatings, corresponding to the conceptual design, can be seen from a comparison of critical loads shown in Fig. 12. The composite toughness was increased by four times in comparison with stoichiometric TiC and by six times in comparison with superhard DLC. It was noted that the critical load for the $Ti_{0.32}C_{0.68}$ coating occurred at contact stresses of almost 10 GPa (Fig. 12).

The mechanism responsible for toughness improvement was investigated with SEM imaging of scratches made at 50 N normal load (about 6 GPa contact stress). Composite coatings with $Ti_{0.41}C_{0.59}$ stoichiometry, a-C interfaces 2 nm thick and about 15 vol% a-C phase, were compared with $Ti_{0.32}C_{0.68}$ coatings, having structural characteristics matching the conceptual design (Fig. 13).

For $Ti_{0.41}C_{0.59}$ coatings, cohesion and adhesion failure by the development of catastrophic macrocracks was observed (Fig. 13a). There was a network of cracks (Fig. 13c), which were propagating along nanocrystal borders (Fig. 13e). In contrast, tough $Ti_{0.32}C_{0.68}$ coatings exhibited parallel nanocracks and microcracks, reflecting the direction of the pseudoplastic compliance (Fig. 13b). These cracks were not connected (Fig. 13d) and terminated in the a-C phase interface between round TiC grains (Fig. 13f).

The pseudoplasticity of the designed composites prevented the build-up of localized stresses and permitted adaptation to the extreme loading without

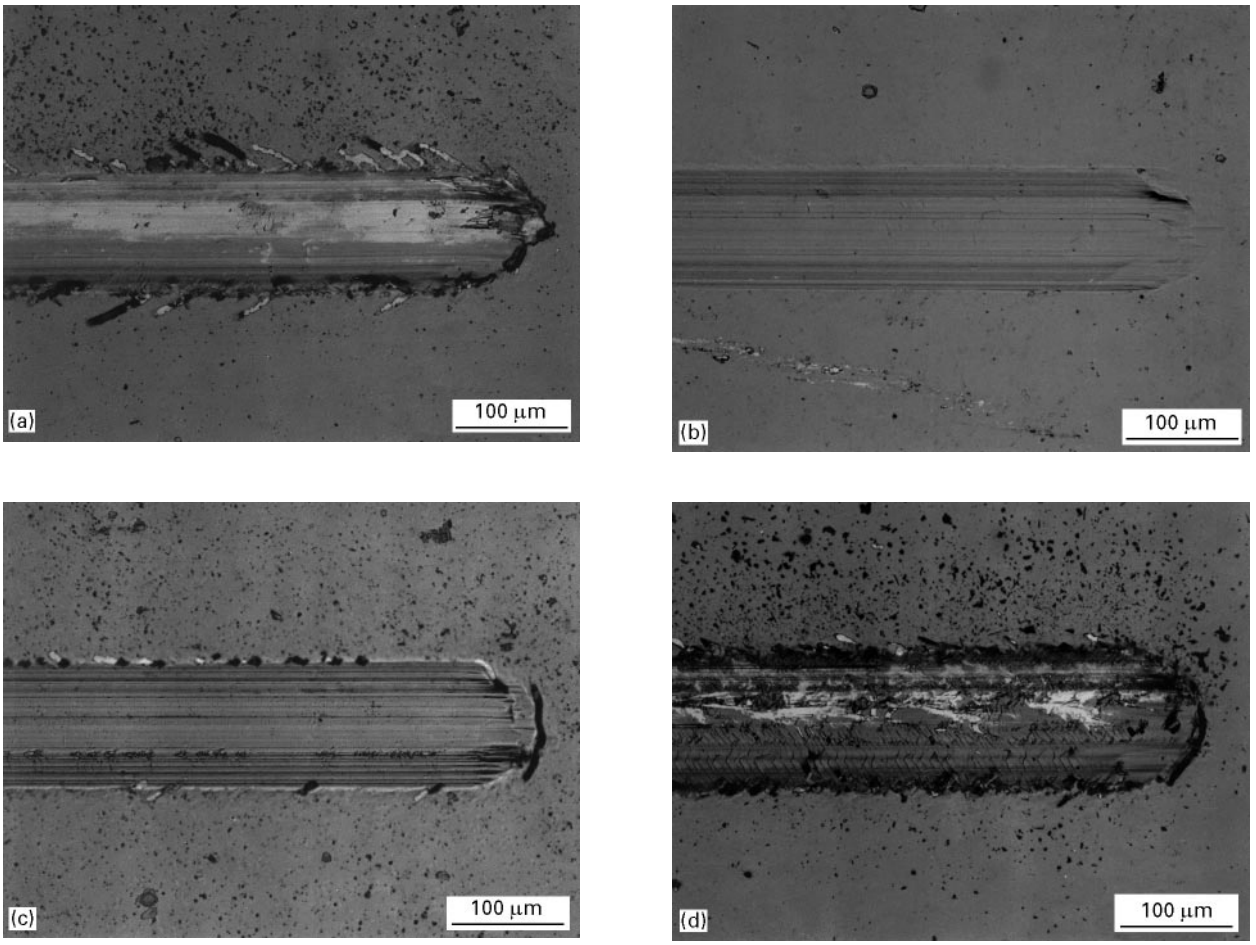

Figure 11 Optical photographs of scratch paths performed on TiC–a-C composite coatings with different carbon contents: (a) 59 at%; (b) 68 at%; (c) 81 at%; (d) 92 at%. The end of the scratch paths correspond to a 50 N normal load. A diamond stylus of 0.2 mm radius was moved from left to right.

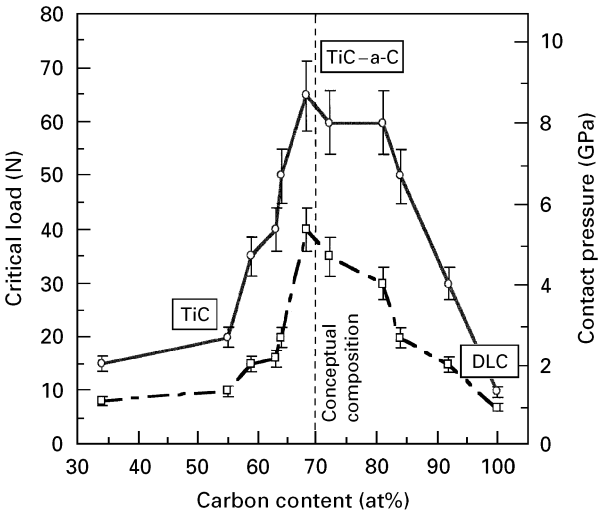

Figure 12 Variation in the toughness of TiC–a-C composites as a function of carbon content. Two scales are used for toughness qualification; the left-hand scale is the absolute value of the critical load of cohesive (— - -□- - —) and adhesive (—○—) strengths, and the right-hand scale is the contact stress induced in scratch path.

brittle fracture. This self-adjustment provided super-tough characteristics, unachievable in single-phase materials or composites designed for superhardness.

5. Summary and conclusions

Nanocrystalline–amorphous composite coatings can be produced with a unique combination of high hardness and toughness, if their structure is designed to prevent brittle failure. In the design proposed, nanocrystals of 10–50 nm size were encapsulated in an amorphous phase, separating the nanocrystals by 5 nm. This permitted generation of dislocation and grain boundary microcracks and nanocracks, which terminated in the surrounding amorphous matrix. The design achieved a self-adjustment in composite deformation from hard elastic to plastic at loads exceeding the elastic limit, as opposed to hard elastic to brittle fracture.

The concept of a load-adaptive composite was realized using the TiC–a-C system. It was based on developments in MSPLD, which permitted the growth of TiC nanocrystals in an a-C matrix at near room temperature. For the conceptual TiC–a-C composites, a fourfold increase in toughness was found in comparison with nanocrystalline TiC, and a more than sixfold increase in comparison with DLC in tests simulating highly localized extreme loading. These properties are beneficial for wear-resistant applications. They can be further enhanced by the a-C potential for solid lubrication, which requires additional studies.

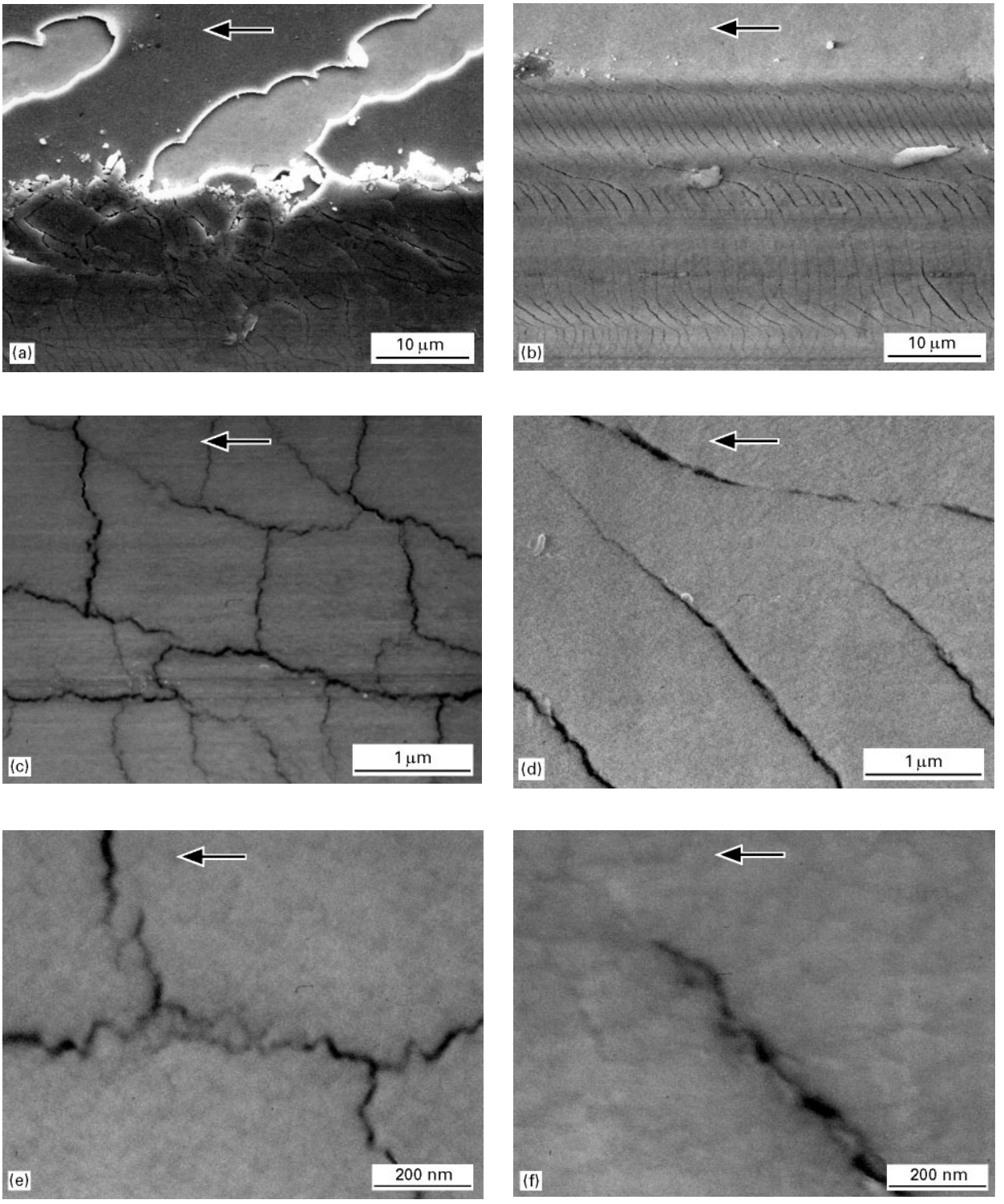

Figure 13 SEM images inside scratch paths on (a), (c), (f) $Ti_{0.41}C_{0.59}$ and (b), (d), (e) $Ti_{0.32}C_{0.68}$ coatings taken at three different magnifications. The $Ti_{0.32}C_{0.68}$ coating corresponds to a designed tough TiC–a-C composite. The arrows indicate the sliding direction of a diamond stylus at 50 N normal load.

Acknowledgements

The authors gratefully thank Dr E. Iarve of the Composite Section, Structural Materials Branch, and Dr S. Prasad of the Tribology Section, Nonstructural Materials Branch, Wright Laboratory, Wright–Patterson Air Force Base, for their useful comments.

References

1. S. VEPREK, M. HAUSSMANN, and S. REIPRICH, *J. Vac. Sci. Technol. A* **4** (1996) 46.
2. S. VEPREK and S. REIPRICH, *Thin Solid Films* **268** (1995) 64.
3. J. -E. SUNDGREN, B. -O. JOHANSON and S. -E. KARLSSON, *ibid.* **105** (1983) 353.
4. O. KNOTEK, E. LUGSCHEIDER, F. LOFFER, B. BOSSERHOFF and S. SCHMITZ, *Mater. Sci. Engng* **A209** (1996) 394.
5. H. DIMIGEN and C. -P. KLAGES, *Surf. Coatings Technol.* **49** (1991) 543.
6. M. WANG, K. SCHIDT, K. REICHELT, H. DIMIGIN and H. HUBSCH, *J. Mater. Res.* **7** (1992) 667.
7. A. A. VOEVODIN, R. BANTLE and A. MATTHEWS, *Wear* **185** (1995) 151.

8. A. A. VOEVODIN, M. A. CAPANO, A. J. SAFRIET, M. S. DONLEY and J. S. ZABINSKI, *Appl. Phys. Lett*. **69** (1996) 188.
9. M. A. CAPANO, A. A. VOEVODIN, J. E. BULTMAN and J. S. ZABINSKI, *Scripta Mater*. **36** (1997) 1101.
10. A. A. VOEVODIN and M. S. DONLEY, *Surf. Coatings Technol.* **82** (1996) 199.
11. A. A. VOEVODIN, M. S. DONLEY, J. S. ZABINSKI and J. E. BULTMAN, *ibid.* **77** (1995) 534.
12. A. A. VOEVODIN, S. D. WALCK, J. S. SOLOMON, P. J. JOHN, D. C. INGRAM, J. S. ZABINSKI and M. S. DONLEY, *J. Vac. Sci. Technol. A* **14** (1996) 1927.
13. A. A. VOEVODIN, M. A. CAPANO, S. J. P. LAUBE, M. S. DONLEY and J. S. ZABINSKI, *Thin Solid Films* **298** (1997) 107.
14. M. N. GARDOS, *Tribol. Trans.* **31** (1990) 209.
15. S. V. PRASAD and J. S. ZABINSKI, *Wear* (1997) **203**/**204** (1998) 498.
16. H. GLEITER, *Prog. Mater. Sci.* **13** (1989) 223.
17. G. E. DEITER, "Mechanical Metallurgy" (McGraw-Hill, New York, 1976) p. 253.
18. W. C. OLIVER and G. M. PHARR, *J. Mater. Res.* **7** (1992) 1564.
19. J. VALLI, U. MAKELA and A. MATTHEWS, *Surf. Engng.* **2** (1986) 49.
20. D. BEEMAN, J. SILVERMAN, R. LYNDS and M. R. ANDERSON, *Phys. Rev. B* **30** (1984) 870.
21. D. S. KNIGHT and W. B. WHITE, *J. Mater. Res.* **2** (1989) 385.
22. P. V. HUONG, *Diamond Relat. Mater*. **1** (1991) 33.
23. S. PRAWER, K. W. NUGENT, Y. LIFSHITZ, G. D. LEMPERT, E. GROSSMAN, J. KULIK, I. AVIGAL and R. KALISH, *ibid.* **5** (1996) 433.
24. A. RICHTER, H. -I. SCHEIBE, W. POMPE, K. W. BRZEZINKA and I. MÜHLING, *J. Non-Cryst. Solids* **88** (1986) 131.
25. A. A. VOEVODIN, S. J. P. LAUBE, S. D. WALCK, J. S. SOLOMON, M. S. DONLEY and J. S. ZABINSKI, *J. Appl. Phys.* **78** (1995) 4123.
26. D. R. LIDE (ed.), "CRC handbook of chemistry and physics" (CRC Press, Boca Raton, FL, 1991) pp. 4–50, 4–108.

Received 17 January
and accepted 30 July 1997